Title

Slickenline orientations as a record of fault rock rheology

Authors

Kirkpatrick, James D
Brodsky, Emily E

Publication Date

2014

DOI

10.1016/j.epsl.2014.09.040

Peer reviewed

Earth and Planetary Science Letters 408 (2014) 24–34

Contents lists available at ScienceDirect

Earth and Planetary Science Letters

www.elsevier.com/locate/epsl

Slickenline orientations as a record of fault rock rheology

James D. Kirkpatrick [a,*], Emily E. Brodsky [b]

[a] Department of Geosciences, Colorado State University, United States
[b] Earth and Planetary Sciences, University of California, Santa Cruz, United States

ARTICLE INFO

Article history:
Received 11 April 2014
Received in revised form 12 September 2014
Accepted 16 September 2014
Available online 22 October 2014
Editor: P. Shearer

Keywords:
fault roughness
stress
slickenline
asperity
fault rock rheology

ABSTRACT

Contact of geometric asperities across rough faults causes perturbations to the shear traction resolved on a fault surface that could potentially deflect the local slip direction. Slickenlines, which record the relative displacement of opposing sides of a fault, may therefore be sensitive to fault surface geometry. To investigate the relationship between fault geometry, shear traction and slip, we use ground-based LiDAR to measure the orientations of slickenlines defined by centimeter-amplitude corrugations on three fault surfaces. Slickenline rakes measured in the mean plane of each fault rarely vary by more than a few degrees. Deviations from the mean rake do not correlate with the fault surface topography at scales up to a few meters, but a weak correlation may be present at larger scales. Slip directions are therefore insensitive to any shear traction perturbations from the contact of geometric asperities at small scales. This observation is consistent with scale-dependent deformation. We show that the roughness of fault surfaces implies that short wavelength asperities fail inelastically because of flattening during fault slip. A crossover to elastic deformation occurs at lengths of 10^{-2} to 10^{0} m, which defines the minimum dimension of a strength asperity that influences the displacement field. The roughness at the crossover length scale corresponds to the typical thickness of fault rocks in the fault core suggesting that fault rock thickness is related to the crossover length scale. The data requires that multiple processes combine to produce the fault surface geometry. We reconcile the variety of processes with the consistent surface roughness scaling by noting that all of the processes are governed in different ways by the elastic limit of rock.

1. Introduction

Fault slickensides display an array of tool marks, corrugations, intersecting fractures, scoops and mullions. These features are used as kinematic indicators that record the relative motion of opposing sides of a fault (Petit, 1987; Doblas, 1998). Together, they define the shape of a fault surface, which for a large variety of faults has been shown to be non-planar at all scales of observation with increasingly large geometric asperities (bumps in the topography of the fault surface) with increasing length scale (Brown and Scholz, 1985; Power et al., 1987; Lee and Bruhn, 1996; Renard et al., 2006; Sagy et al., 2007; Sagy and Brodsky, 2009; Candela et al., 2009, 2012; Fondriest et al., 2013; Siman-Tov et al., 2013). Fault surface roughness is typically described as self-affine, implying that ratio of asperity amplitude to wavelength is a power law function of the scale of observation. In the case of faults, the ratio decreases as a function of increasing length scale.

During slip on a well-matched fault, asperities on the surface form local restraining and releasing zones. Slip zones defining slickensides are often located at the boundary between damaged wall rock and fault rock (e.g. Sagy and Brodsky, 2009; Caine et al., 2010; Kirkpatrick et al., 2013), may be localized within a fault core (e.g. Chester and Chester, 1998; Katz et al., 2003; Chambon et al., 2006), and occasionally are inferred to have developed in intact rock (e.g. Di Toro and Pennacchioni, 2004). Slickenfibers developed on some slickensides suggest small-scale opening at dilational steps, but faults rarely contain voids or other evidence of significant separation across fault surfaces. Contact of asperities is integral to fault rock development, which is thought to be a wear process involving either elastic or inelastic failure of asperities defined by the shape of the slickenside (e.g. Archard, 1953; Greenwood and Williamson, 1966; Scholz and Engelder, 1976; Power et al., 1988; Lyakhovsky et al., 2014). Failure of the rock surrounding a self-affine fault surface, whether the wall rock is intact or is composed of fault rock, is predicted to occur after slip

* Corresponding author.
E-mail address: james.kirkpatrick@colostate.edu (J.D. Kirkpatrick).

http://dx.doi.org/10.1016/j.epsl.2014.09.040

amounts of 10^{-1} m or less depending on the amplitude: wavelength ratio of the asperities (Sagy and Brodsky, 2009).

Fault slip is therefore inherently dependent on the interaction of rough fault surfaces. Analytical and numerical models show that these interactions induce stress heterogeneity in the wall rock and the material inside the fault zone (Saucier et al., 1992; Chester and Chester, 2000; Dunham et al., 2011; Shi and Day, 2013). Fault surface shear traction variations can arise from a number of effects (Pollard et al., 1993) but the stress perturbations caused by elastic asperity collisions are thought to be large compared to the compressional strength of intact rock (Sagy and Brodsky, 2009), suggesting that the interaction of asperities on fault surfaces should cause the resolved shear traction orientation and magnitude to be spatially variable (Marshall and Morris, 2012).

Perturbations arising from asperity contact to an otherwise uniform shear traction direction defined by the tectonic stress field are thought to be sufficiently large to affect the resulting fault slip distributions (e.g. Dieterich and Smith, 2009; Resor and Meer, 2009; Sagy and Brodsky, 2009; Shen et al., 2009; Marshall and Morris, 2012; Ritz and Pollard, 2012). This implies that slickenlines, which form as one side of a fault moves past another and record fault slip vectors, should change orientation over a rough fault surface. A correlation between the slickenline direction and the orientation of the maximum resolved shear traction is one of the central assumptions of methods that estimate the far field stress tensor from fault surface observations (e.g. Bott, 1959; Angelier, 1989; Reches, 1987; Gephart, 1990). However, these approaches associate the average slip direction with the average shear traction direction and do not take account of local variability arising from fault topography.

In this study, we aim to measure the orientations of slickenlines over a large area of several fault slickensides to test the effect of the non-planar fault topography on displacement directions. We use ground based LiDAR to measure the deviation of slickenlines from the mean orientation on the fault and couple the measurements with analysis of the slickenside geometry. We develop a new method for identifying and measuring slickenlines in a typical terrestrial laser scanner point cloud, and use the method to test whether slickenlines can be found from the curvature of a fault surface (*cf.* Jones et al., 2009; Resor and Meer, 2009). The results provide an observational constraint on whether the shear traction perturbations caused by asperities are matched by changes in the slip vector orientation.

2. Study site: the Corona Heights fault

We focus on the Corona Heights fault, San Francisco, USA, a subvertical structure that cuts a chert body within the Marin Headlands terrane of the Franciscan complex (Blake et al., 1984; Murchey and Jones, 1984). The chert body is ~500 m in diameter, and consists of well-bedded (~10–20 cm beds) homogeneous radiolarian chert with a total stratigraphic thickness of ~80 m (Murchey, 1984). Deformation conditions for the Corona Heights fault are difficult to establish because the chert lacks metamorphic indicators. The best constraint is from observations of amorphous and intermediate crystalline phases of silica in a vitreous layer covering the fault slickenside that show the fault rocks formed on a retrograde path at temperatures less than ~100 °C during San Andreas deformation (Kirkpatrick et al., 2013).

The Corona Heights fault is exposed as a large slickenside (~60 × 15 m) in the Corona Heights Park with an average orientation of 239/78° NW (Candela et al., 2009; Kirkpatrick et al., 2013; Fig. 1). Due to a lack of exposed piercing points, the total offset is poorly constrained. Considering the ~80 m stratigraphic thickness of the chert and the 27° NE rake of the slip vector on a subvertical fault (see below) the presence of chert on both sides of the fault constrains slip to <120 m. However, although the mapped fault trace is ~380 m long, no offset is obvious from the macroscopic shape of the chert body (Blake et al., 2000), suggesting the total slip is more likely of the order of 50 m or less. These estimates are consistent with displacements expected from scaling relations based on the trace length of the fault (e.g. Cowie and Scholz, 1992).

The exposed fault surface is rough at all scales of observation (Fig. 1). Small-scale features include grooves in the vitreous layer on the slickenside, intersections of synthetic fractures with the slickenside, and the non-planar shape of the vitreous layer surface. Intermediate-scale structures are corrugations with cm-scale amplitudes composed of cataclasites cut by synthetic shear fractures (Kirkpatrick et al., 2013). These corrugations are linear features that can be traced for several meters or more across the fault and are commonly utilized as slickenlines. They have irregular shapes in cross section with steep sides and flat tops and are spaced every few tens of centimeters perpendicular to their long axes (Fig. 1c). These corrugations are the slickenlines that are the focus of this study. At larger scales, amplitudes of large semi-ellipsoidal asperities on the exposed surface reach ~1 m. Tool marks, steps and asymmetric profiles of asperities on the fault surface are all consistent with dextral shear.

Decomposing the Corona Heights fault surface geometry into its spectral components produces a power spectrum that can be fit by a power law over a range of wavelengths with a slope <3 (Fig. 1f; Candela et al., 2009, 2011a). Different scaling exponents in the slip parallel and slip perpendicular directions show the surface roughness is anisotropic. The constant power law fits over wavelengths from millimeters to meters indicates that asperities exist at all observed scales on the fault surface.

Fault rocks within the Corona Heights fault are cohesive cataclasites that form a fault core approximately 10–20 cm thick (Fig. 1d). The cataclasites are made up of μm- to cm-long, angular to sub-rounded clasts of chert with no preferred orientation. Some clasts contain previously formed cataclasite indicating multiple slip events on the fault. Subsidiary synthetic shear fractures cut the cataclasites, intersecting the slickenside surface along arcuate traces. The vitreous layer on the slickenside surface corresponds to the fault principal slip zone. It is ~1–3 mm thick and contains μm to sub-μm quartz, hydrous amorphous silica and Fe-oxide grains (Kirkpatrick et al., 2013).

3. Measuring slickenlines with LiDAR

The three-dimensional shape of the Corona Heights fault surface was measured with a Leica HDS3000 ground-based LiDAR (Light Detecting And Range) instrument (Fig. 2). The fault surface was scanned at a distance of ~15 m with an average point spacing, dx, of ~7 mm. Range error for each data point is ~3 mm (Sagy et al., 2007). The scan was cleaned to remove noise and unwanted objects and the cleaned data was rotated so that the mean plane through the fault was horizontal, in a reference frame with a vertical, fault-normal z-axis, and x-axis and y-axis contained in the mean plane of the fault.

3.1. Slickenlines defined by tape

In order to identify corrugations on the fault surface as slickenlines in the LiDAR point cloud, 302 pieces of duct tape were applied to the Corona Heights fault surface prior to scanning. The reflectivity of the tape is different to that of rock, so the tape can be detected in a LiDAR point cloud from the intensity of the signal returned to the scanner. The edge of each piece of tape was aligned with a well-preserved slickenline defined by a corrugation (Fig. 2). Pieces of tape were ~0.3–1 m long, and the slickenlines were chosen where they were continuous over lengths greater than ~1 m.

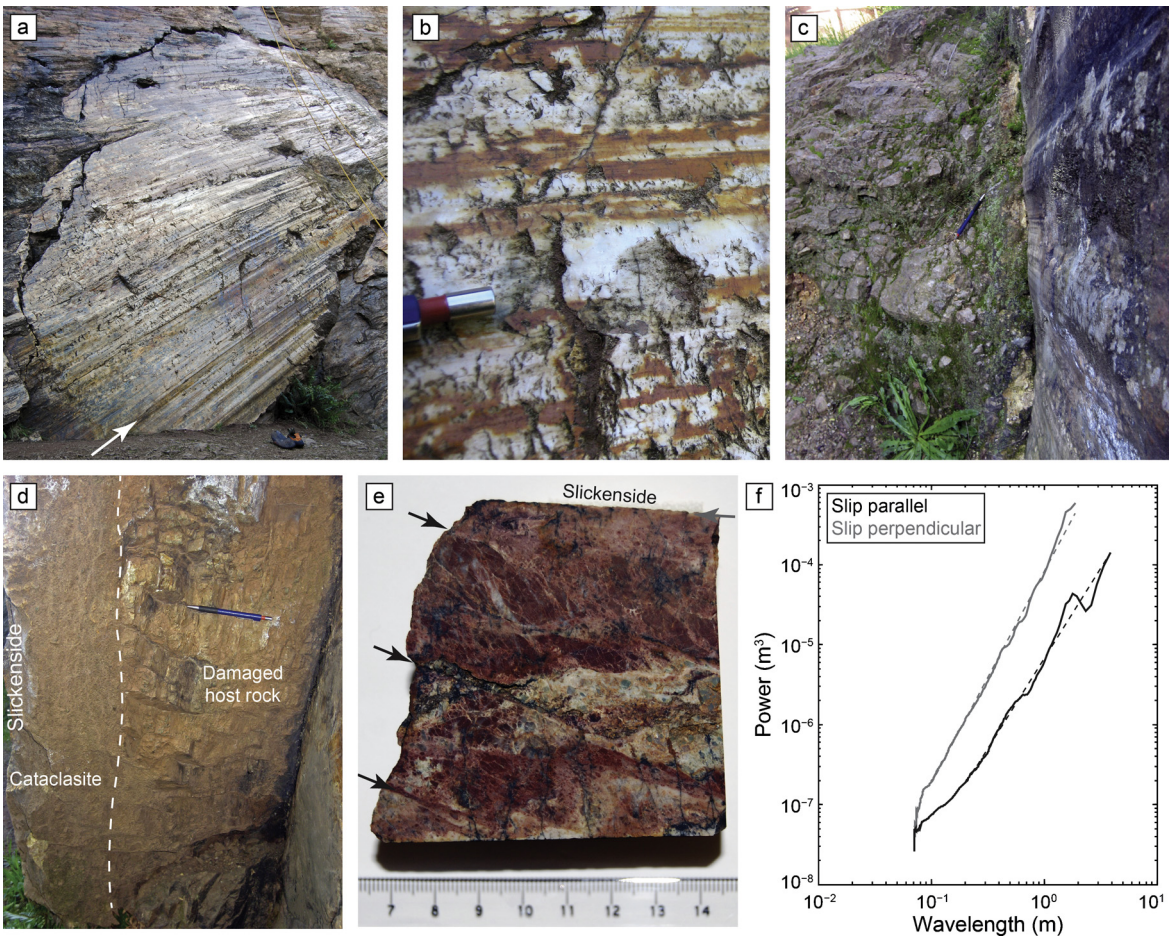

Fig. 1. a. Part of the slickenside of the Corona Heights fault showing the vitreous surface, overall shape of the slickenside and slickenlines defined by corrugations (view approximately to the south). The fault surface shown here has an average orientation of 059/78° NW and the corrugations rake 27° NE (shown by white arrow). b. Detail of the surface showing kinematic indicators consistent with dextral slip. c. View down-plunge of the corrugations showing their elliptical or flat-topped profiles. d. Photograph looking along strike towards the NE showing the structure of the fault behind the slickenside. Note the thickness of cataclasite adjacent to the slickenside e. Hand specimen of fault rock from adjacent to the slickenside cut approximately perpendicular to the fault plane and parallel to the slip vector. Angular fragments of varicolored chert between synthetic shears (black arrows) are cemented by quartz, and in a mm-thick layer adjacent to the slickenside, amorphous silica (grey arrow). f. The power spectral density of the Corona Heights fault surface. Dashed lines are the best-fit power law in each direction. The slopes, β, are 2.25 ± 0.022 in the slip-parallel direction and 2.65 ± 0.012 in the slip-perpendicular direction.

We defined the slickenlines by filtering the LiDAR data according to the intensity value and isolating each resulting linear point cloud corresponding to duct tape (Fig. 2). As tape has negligible thickness compared to the precision of the LiDAR scanner, the slickenline measurements are co-located with the fault surface.

3.2. Slickenlines defined by curvature

In addition to the duct tape analysis, we defined slickenlines by analyzing the curvature of the fault surface (Bergbauer and Pollard, 2003; Jones et al., 2009; Resor and Meer, 2009). Corrugations on the Corona Heights fault surface have non-uniform curvature, with high values adjacent to low values at the flat corrugation tops defining a characteristic pattern. However, fractures and other irregularities in the surface also result in locally high curvatures. To minimize noise in the curvature analyses, we removed as many broken or eroded parts of the fault surface as possible (around half of the LiDAR data points were removed). We also performed an additional rotation of the resulting data set around the z-axis to align the corrugations with the x-axis for calculation of the Fourier power spectral density of the cleaned fault surface (see Fig. 1f).

Curvature was calculated following Bergbauer and Pollard (2003). We chose to focus on the principal curvature directions as a representation of the shape of the fault surface, as they provided the clearest definition of the corrugations. The re-gridded fault topography was smoothed using a weighted running average of the re-gridded z values over a window of ten data points. The frequency of the corrugations on the fault surface (for the Corona Heights fault: 10^1 m^{-1}) is lower than both the data Nyquist frequency and the smoothing window size (10^3 m^{-1} and 10^{-2} m^{-1} respectively), allowing analysis of the curvature of these relatively high frequency structures in the data. The principal curvature directions were calculated (Eq. (9) of Bergbauer and Pollard (2003) and the preferred first principal curvature direction picked using a moving window autocorrelation function with a window approximately three corrugation wavelengths in dimension.

We extended our analyses by measuring slickenline orientations from the curvature of two additional faults where the duct tape method was not employed: the Dixie Valley fault (Nevada, USA) and the Arkitsa fault (Greece). The Dixie Valley fault is a seismogenic normal fault with 3–6 km throw. At the study location, the 'Mirrors locality' (Power et al., 1987, 1988; Candela et al., 2011b), a complex array of polished slickensides of hydrothermal silica with dips from ~30° to 70° overlie a granodiorite footwall (Caine et al., 2010). Slickenlines rake moderately steeply (average ~65° NE) but are variable (Caine et al., 2010). The Arkitsa fault is also a seismogenic normal fault (dip ~60°) that juxtaposes Mesozoic carbonates in the footwall and Neogene sediments and colluvium in

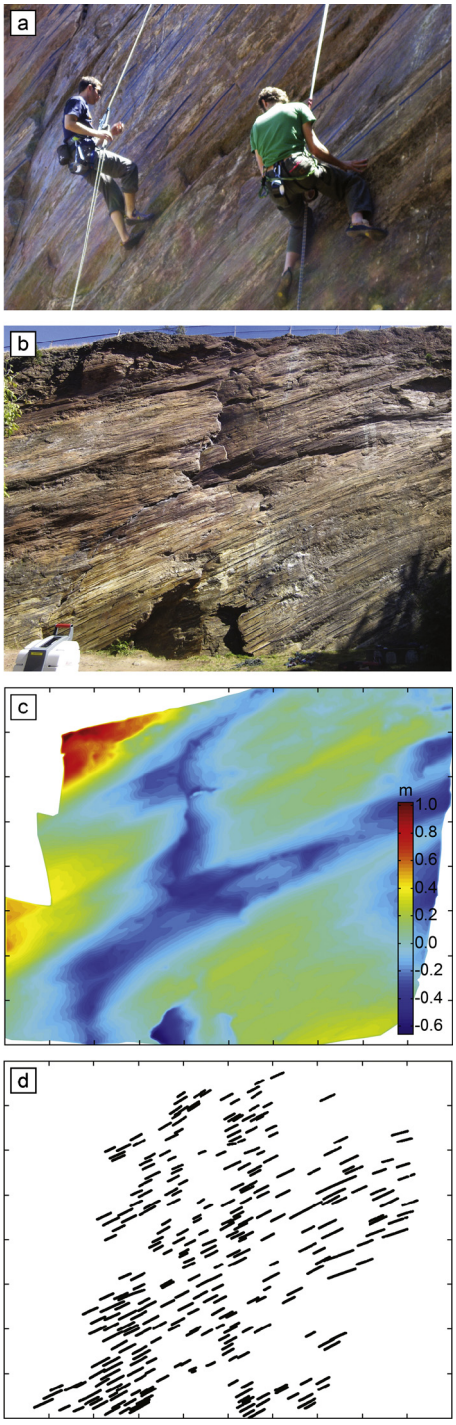

Fig. 2. a. Photograph showing ~0.3–1 m long pieces of duct tape being applied to the Corona Heights fault surface parallel to corrugations. b. Photograph of the fault slickenside showing the area of the fault surface scanned with the LiDAR (the laser scanner is shown in the foreground). Note the black lines over the exposure are the pieces of duct tape. c. Map of the fault surface topography defined by the re-gridded point cloud. The colors represent the distance of a point from the mean plane through data, warm colors are closer to the scanner. Large asperities with long axes plunging down to the left in this view can be seen. d. Linear point clouds defined by filtering the point cloud according to the intensity of the signal returned to the scanner from the surface. These point clouds correspond to pieces of duct tape applied to the slickenside. (For interpretation of the references to color in this figure legend, the reader is referred to the web version of this article.)

the hanging wall (Jackson and McKenzie, 1999). The north-dipping, polished slickenside overlies a cemented zone of fault breccias ~1 m thick. Slickenlines on the surface rake ~65° W (Resor and Meer, 2009). These faults were scanned and analyzed for roughness properties during several earlier studies (Jones et al., 2009; Candela et al., 2011b). The average point spacing is different for each fault: Dixie Valley fault, $dx \sim 0.003$ m; Arkitsa fault, $dx \sim 0.04$ m. We followed the above procedure for smoothing the data and calculating curvature, but the minimum wavelength structure that is resolved in each data set is different.

4. Slickenline rakes

4.1. Measurements from tape: the Corona Heights fault

Slickenline orientations were measured from the LiDAR data by fitting a best-fit curve through each linear point cloud corresponding to duct tape in the mean plane of the fault. A least-squares regression was used, with each linear point cloud comprising 50 to 1000 points. The rake of each slickenline in the mean plane of the fault was defined as the angle of the line to the x-axis, with maximum errors of approximately ±3° for point clouds with very few data points, though we expect these to be <1° for the majority of the measurements because the number of points in each point cloud is large.

The pieces of tape show that the slickenlines are generally subparallel over the fault surface (Fig. 3a). Only a few instances of slickenlines at different angles were observed. The mean slickenline rake defined in the LiDAR dataset is 27.01° (±2.45° 1σ, $n = 302$) to the northeast (Fig. 3b). We verified the LiDAR results by comparing them to measurements made in the field that yielded a mean rake of 26.9° (±2.7° 1σ, $n = 30$) to the northeast.

Deflections, defined as the difference between the local slickenline rake and mean of the entire population, are upward (negative) or downward (positive) relative to the mean and range from 9.78° to −23.12°, with a standard deviation of 4.28° (Fig. 3a, d). Comparing the slickenline rake to the local fault topography shows that there is no correlation between the magnitude of the deflection and the height of the slickenline measurement on the rotated fault plane (Fig. 3c). Furthermore, there is no correlation between the magnitude of the deflection and the plunge of the normal to the fault surface when projected into the slip direction-z plane (Fig. 3d), as has been observed previously (Resor and Meer, 2009).

4.2. Measurements from curvature

The first principal curvature directions show bands of constant orientation that extend across the entire scanned area of the Corona Heights fault. Slickenlines defined by duct tape are parallel to this fabric in the first principal curvature field (Fig. 4b, c), showing that the curvature provides a good representation of the slickenlines. This is supported by the autocorrelation analysis of the curvature field that shows an extremely similar rake deflection distribution to the deflections calculated from the tape (deflections in the curvature measurements were ±3.91° 1σ, $n = 714$).

Slickenlines defined by curvature for the other two faults we studied have similar characteristics to those of the Corona Heights fault. The curvature of the Dixie fault surface shows a clear fabric in the first principal curvature direction field (Fig. 5). Although the size of the scanned area is roughly one quarter that of the Corona Heights fault, few of the bands of constant first principal curvature direction are continuous across the whole exposure. Slickenlines show a narrow range of orientations: the variation in rake is restricted to ± 2.09° (1σ, $n = 541$).

Corrugations with wavelengths of approximately 0.5 m on the Arkitsa fault surface can be seen to extend almost continuously over tens of meters (Jackson and McKenzie, 1999; Jones et al., 2009; Resor and Meer, 2009). Deflections of these slickenlines defined by curvature on the Arkitsa fault are ± 2.58° (1σ, $n = 681$; Fig. 6). These results are comparable to those published previously

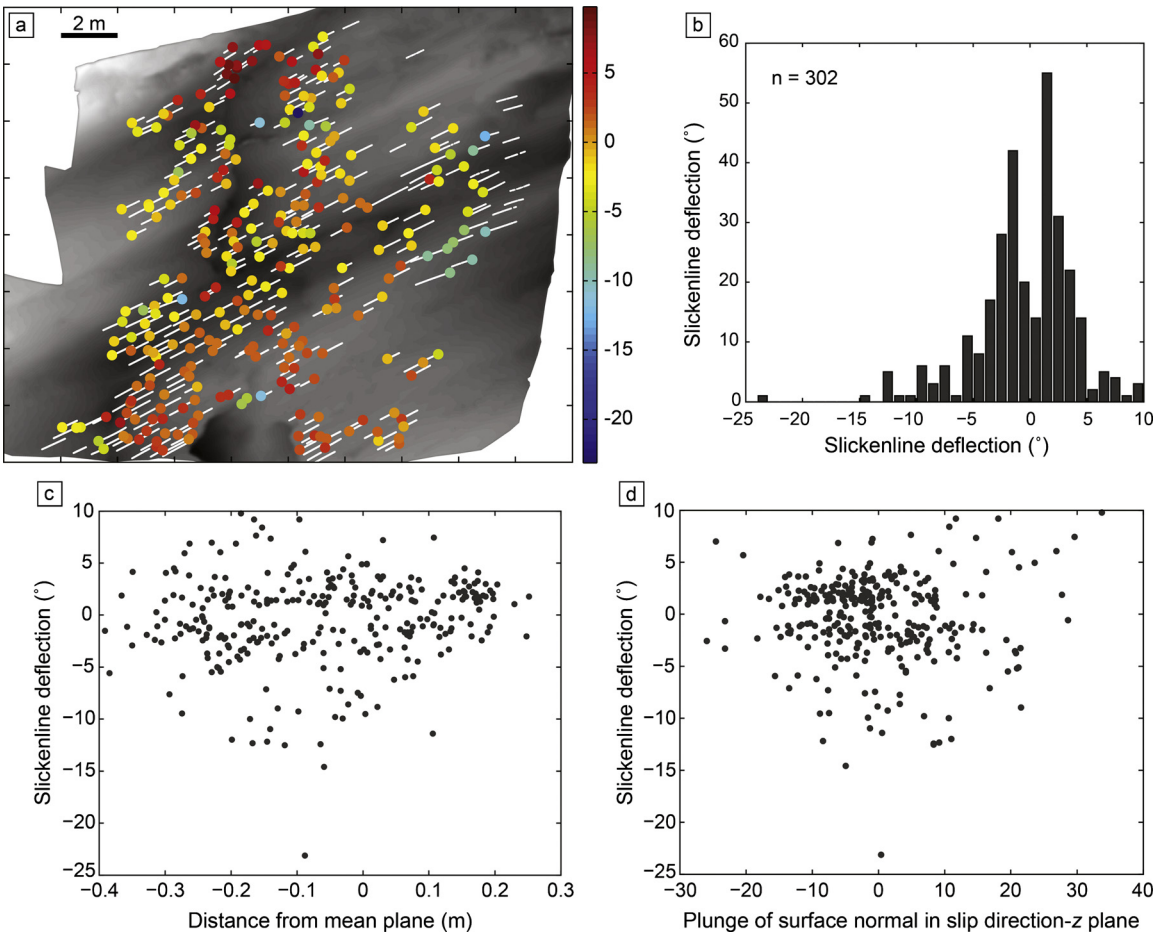

Fig. 3. a. Slickenlines defined by point clouds corresponding to duct tape (white lines) and the deflection of the slickenline rake away from the mean rake for the population (colored circles). The deflection is generally small ($1\sigma = 4.28°$) and upwards and downwards deflections are spatially mixed. b. Histogram showing the measured slickenline deflections. c. Plot showing the magnitude of deflection as a function of the distance from the fault mean plane. d. Plot showing the deflection as a function of the plunge of the fault surface when projected into the plane normal to the fault surface and containing the slip direction measured locally at the slickenline rake measurement. (For interpretation of the references to color in this figure legend, the reader is referred to the web version of this article.)

using a different method of extracting a slip vector orientation, suggesting the method we employed to analyze the high frequency component of the surface roughness provides robust results (Jones et al., 2009).

4.3. Large-scale spatial distribution of rake deflections

Deflections greater than 1 standard deviation from the mean in the Corona Heights curvature data set tend to be located in the troughs on the fault surface as viewed in the exposure, and the most positively and negatively deflected rakes tend to be clustered into separate groups (Fig. 7). For example, white circles with black outlines are clustered on the right hand side of Fig. 7. Black circles with white outlines are clustered on the lee side (for the dextral fault) of an asperity on the left of Fig. 7. There is a cluster of white circles on the right of Fig. 7 that are in between the largest asperities on the surface. Elsewhere the deflection polarities are mixed (e.g. compare red and blue circles in Fig. 3a).

There is a small systematic change in the slickenline rake across the exposure of the Arkitsa fault (Jackson and McKenzie, 1999). Slickenlines to the right (up-dip) of the map of slickenline rakes shown in Fig. 6c are rotated ∼2° counterclockwise with respect to slickenlines to the left (near the base of the exposure). Although this pattern is apparent to the eye, the magnitude of the slickenline rotation is small compared to the spread in the data so is not apparent in the histogram of rake measurements (Fig. 6d). The pairs of arrows and grey lines in Fig. 4b also indicate that there are systematic changes of a few degrees from side to side across the Corona Heights fault exposure.

5. Discussion

The primary objective of this study was to test whether the large geometric asperities visible on fault surfaces cause slickenline directions to vary spatially. Our results show that at the small scales well resolved by the LiDAR datasets the slickenline rakes are consistent over the fault surfaces, and the measured orientations do not appear correspond to any fault geometry control (Fig. 3). However, at larger scales there is weak evidence for systematic slickenline orientation variation, which may result from fault geometry. Below, we use these observations to constrain the potential relationships between fault geometry, shear traction and slip.

5.1. Fault slip and shear traction directions

The slickensides we studied have relief of the order of 0.5 to 5 m, expressed as topographic highs (asperities) and depressions of all sizes on the fault surfaces. The relative displacement of opposing sides of rough fault surfaces induces stresses in the wall rocks if asperities deform elastically to slide by each other (Chester and Chester, 2000; Sagy and Brodsky, 2009; Candela et al., 2011b; Dunham et al., 2011; Marshall and Morris, 2012). These stresses are thought to perturb the tectonic stress field and cause the fault

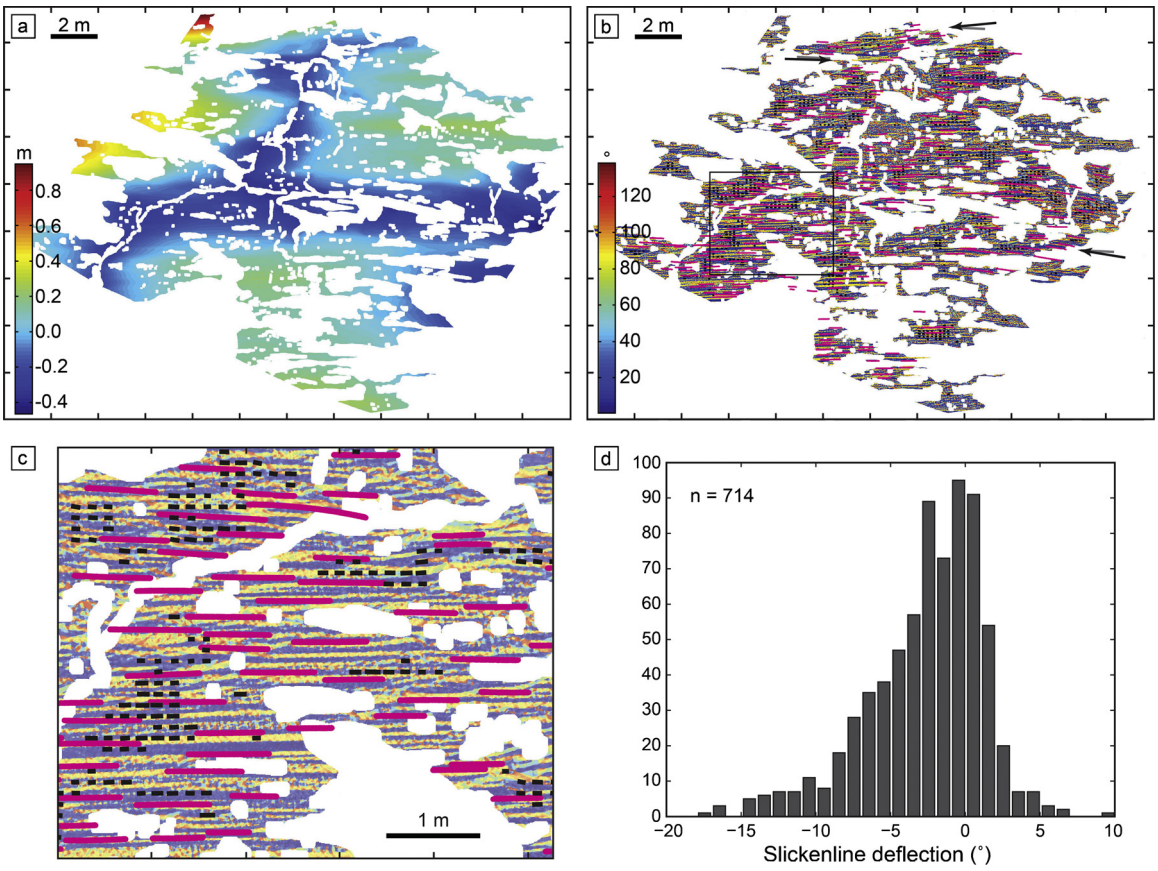

Fig. 4. a. The Corona Heights fault LiDAR point cloud after rotation so the x-axis is slip parallel and after further cleaning removed around half of the points in the original dataset. b. Plot showing the angle the first principal curvature direction makes to the horizontal axis (colors). Note the fabric with horizontal bands of preferred curvature directions. Overlain in pink are the linear point clouds corresponding to duct tape and black dots show the locations where slickenlines were picked using the moving window cross correlation method. Arrows around the edge of the data show the approximate local rake compared to the mean slickenline orientation (grey lines). The location of c. is shown by the box. c. Detail of the first principal curvature directions and slickenlines defined by duct tape (pink bands) and the moving window cross correlation method (black lines). The fabric in the curvature field, the pink bands and black lines are all locally parallel. Color scale for the first principal curvature direction is the same as in b. d. Histogram of rake deflections from the mean orientation as defined by the fault curvature (compare to Fig. 3b.). (For interpretation of the references to color in this figure legend, the reader is referred to the web version of this article.)

surface shear tractions to vary spatially. Although boundary conditions such as the fault finiteness can result in a rotation of the slip direction relative to the shear tractions, for an elastic, isotropic fault zone the superposition principle requires that perturbations to the stress field generate a local rotation of the displacement field (Pollard et al., 1993). It follows that if the slickenlines were locally parallel to the maximum shear traction directions, stresses induced by deformation of the rough fault surfaces would cause deflection of slickenline trajectories.

The small variations in the fault displacement directions indicated by our results may suggest that the stress perturbations due to elastic interactions of asperities are small compared to the combined tectonic stresses and inertia (Dunham et al., 2011; Shi and Day, 2013). However, previous work has shown that the elastic stresses from contact between realistically rough surfaces are expected to be large at small scales (Sagy and Brodsky, 2009). The commonly observed self-affine scaling of surfaces with a power spectral density scaling exponent less than 3 demands unbounded elastic stresses as the scale decreases (Candela et al., 2011b) so the observations are inconsistent with elastic deformation.

An alternative explanation could be incomplete contact between the two sides of the fault during slip due to inertial effects. In this case, the relatively small perturbations to the slip vector would result from reduction of normal stress during sliding. The current generation of numerical models (e.g. Shi and Day, 2013; Fang and Dunham, 2013) is not yet capable of simulating this dynamic and fully 3-D process at the appropriate scale so this possibility must remain in the domain of speculation at the moment.

A third possibility is that inelastic or anisotropic rheology of the fault zone can result in non-parallelism of the stress and displacement field and a lack of superposed solutions (Twiss and Unruh, 1998), in which case the displacement field could be insensitive to shear traction perturbations from fault roughness. We investigate this possibility by analyzing the shape of the fault surface to constrain the effects of deforming asperities during slip. The Corona Heights fault is self-affine (similar to faults in general), with a power spectral density scaling exponent, β, of $\sim$2.25 in the slip-parallel direction (Fig. 1f). This means that the asperity height, H, to length, L, ratio decreases as a function of scale (Fig. 8a).

As an end-member case for the magnitude of the perturbation resulting from the deformation of asperities, we calculate the strain as a function of length scale by assuming all asperities are completely flattened to enable displacement of opposing sides of a fault. Strain, $\varepsilon(L)$, in this scenario is given by H/L. This case is applicable when the slip is much greater than the wavelength L of the initial feature that was correlated across the fault (Chester and Chester, 2000). As the slickenlines we studied can be traced over meters (see Figs. 1, 4 and 6), and we are evaluating the roughness from meters to sub-centimeter topography, this is the relevant limit. The root mean square (RMS) height of an asperity compared to the mean fault plane, $\hat{H}$, at a particular length scale can be

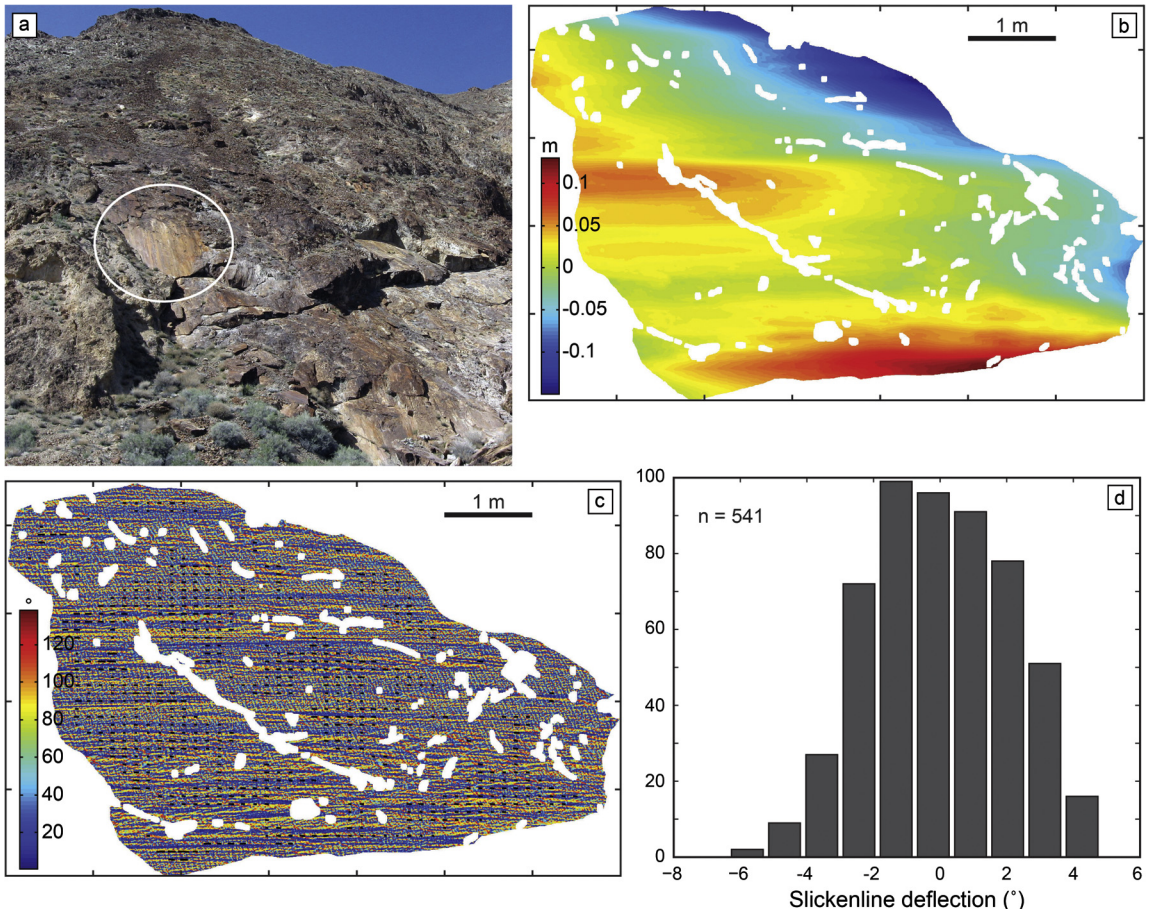

Fig. 5. a. Photo of the exposure of the Dixie Valley fault slickenside, Nevada, which is developed in silicified metagabbro of the footwall to this normal fault (view to the northwest). White ellipse shows the fault surface panel in b. b. Topography of the fault surface (after rotation so the mean plane is horizontal and the slip vector aligned with the *x*-axis). Note the holes in the data are where cracks and other erosional features were removed. c. Map of the first principal curvature direction (measured from the *x*-axis) showing a pronounced horizontal fabric in this field of view. The locations where slickenlines were measured using the moving window cross-correlation analysis were measured. d. Histogram of the deflections of the slickenline rakes from the mean direction measured from the fault curvature.

calculated from β and the power at some reference length scale, $C = p$ $(\lambda = L)$ (Brodsky et al., 2011):

$$\hat{H} = \sqrt{\frac{CL^{\beta-1}}{(\beta-1)}} \tag{1}$$

The exponent $(\beta-1)/2$ defines the self-affine behavior and is called the Hurst exponent, h (in Eq. (1) we correct a typo in Eq. (4) of Brodsky et al., 2011).

Using $\hat{H}$ as an estimate of the height H at each length scale L, we calculate $\hat{H}/L$ for the Corona Heights fault by taking $\beta = 2.25$, and the power C at $\lambda = 1$ m from the power spectral density calculated in the slip-parallel direction (Fig. 1f). The results show that the strain for flattening asperities at short length scales is greater than that for larger length scales (Fig. 8b). Additionally, the magnitudes of strain at short length scales are significantly larger than typically accepted values for the elastic limit of crustal rocks of ~1% (e.g. Means, 1976). This implies that during slip, the flattening of asperities at length scales smaller than some critical value causes the strain in the rock to exceed the elastic limit and therefore deform inelastically, while asperities larger than the critical length scale deform elastically and are able to move past each other without internal failure. According to our measurements of the Corona Heights fault, the expected crossover length scale between these two regimes is $\sim 10^{-1}$ m (Fig. 8b). The crossover length scale could range from 10^{-2} m to 10^{0} m given the typical order of magnitude variation in the prefactor of the power spectral density (Candela et al., 2012).

The above order of magnitude analysis applies to the case of compression of asperities at all length scales. The contact theory developed by Persson (2001) provides the theoretical tools to define and calculate the crossover scale where the real area of contact between self-affine surfaces is a function of scale. Persson (2001) finds an approximate closed form solution for the scale at which a fixed percentage of the asperities yield as a function of the maximum scale of the self-affine topography, L_0. The key result for our analysis is that for all scales smaller than L_0/ζ, if the Hurst exponent is <1, more than half the asperities have yielded. Here, ζ is given by

$$\zeta = \left[1 + \frac{1-h}{h}\left(\frac{2(1-\nu^2)\varepsilon_y L_0}{\pi^2 \hat{H}_0}\right)^2\right]^{\frac{1}{2(1-h)}} \tag{2}$$

where the RMS roughness at scale L_0 is $\hat{H}_0$ and is calculated from Eq. (1), ν is Poisson's ratio and ε_y is the yield stress normalized by the Young's modulus (Persson, 2001; Eq. (C12)). For the observed roughness of the Corona Heights fault ($C = 10^{-5}$; $\beta = 2.25$), an assumed yield strain ε_y of 1%, a Poisson's ratio of 0.25, and the range of L_0 bounded by the length encompassed by the LiDAR data set (~10 m) and the length of the mapped fault trace (380 m), the resulting scale of 50% yielding is 3–6 m. This is compatible with the estimates from Fig. 8 and inference of field-scale yielding.

In summary, the roughness measurements contradict the assumption of elasticity at all scales, and therefore imply that the fault has a more complex rheology. We suggest that the observation that the displacement field was relatively insensitive to any

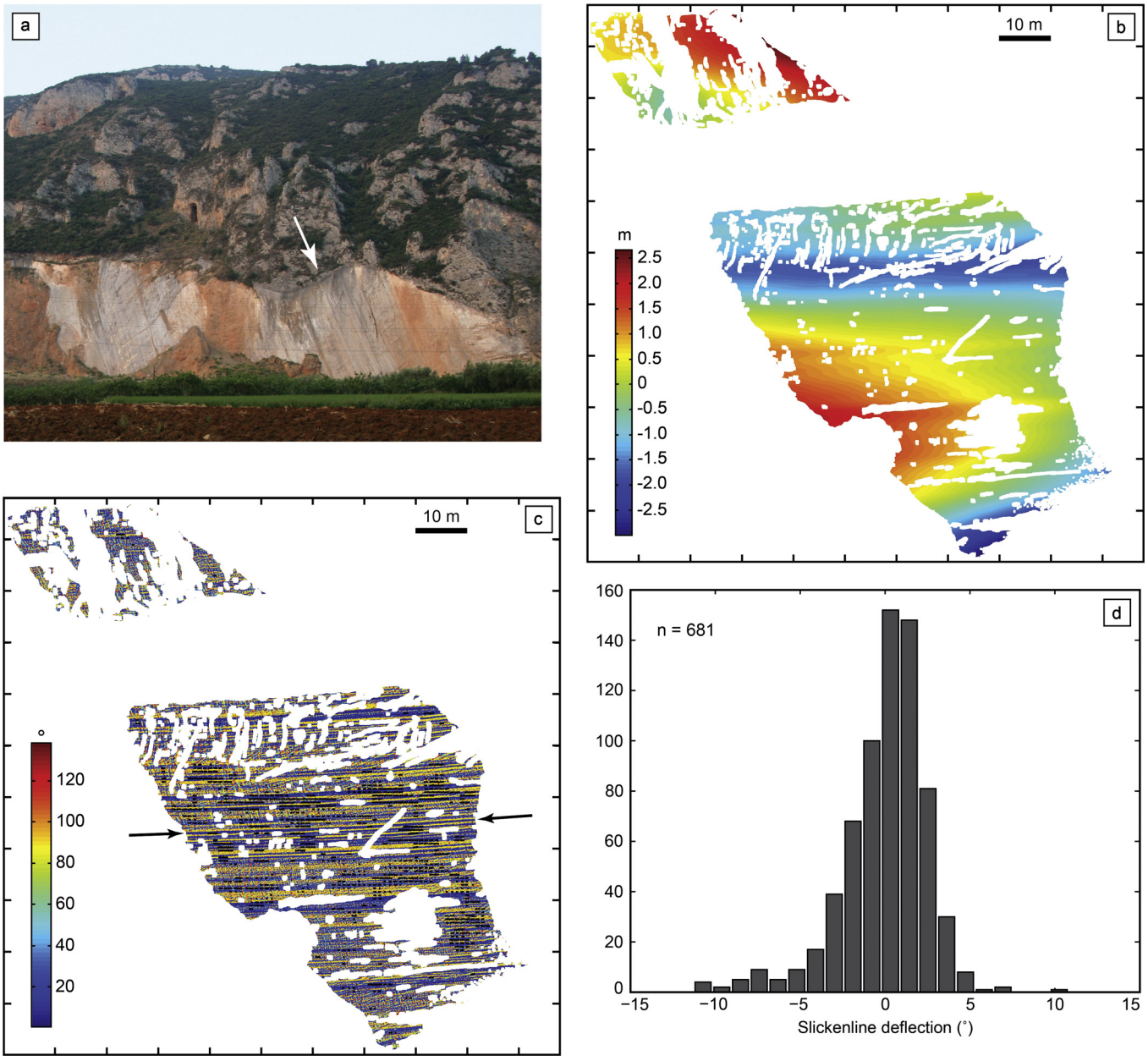

Fig. 6. a. Photograph of the fault slickenside of the Arkitsa fault, Greece, showing prominent corrugations on the fault surface raking steeply from the right in this view (view towards the south; photo courtesy of Phil Resor). The arrow indicates the fault surface we studied (average orientation 301/58° NE; Resor and Meer, 2009). b. Topography of the fault surface defined by the LiDAR point cloud that has been rotated so the mean plane is horizontal, the slip direction is parallel to the *x*-axis and cracks and other erosional features have been removed. c. Map of the first principal curvature direction showing prominent horizontal fabric in this reference frame corresponding to the fault corrugations. Black dots show locations where the slickenline rake was measured. Black arrows show the dominant slickenline rake on the left and right of the map. The right hand arrow is rotated ∼2° counterclockwise from the left arrow. d. Histogram of the deflections of the slickenline rakes from the mean direction as measured from the fault curvature.

perturbations to the fault surface shear tractions can be explained if the material defining asperities up to a critical length scale of approximately several meters was in an inelastic regime during slip (Twiss and Unruh, 1998). In contrast to asperity failure due to contact across nominally flat surfaces that are self-affine over a limited bandwidth (Archard, 1953; Greenwood and Williamson, 1966; Scholz, 1987), the constant scaling over all observed wavelengths of natural faults implies that inelastic deformation is scale-dependent, and suggests wear rates may also be scale-dependent (Power et al., 1988).

The crossover length scale described above defines the minimum size of a strength asperity (region of the fault supporting large stress) where elastic stresses on a fault during slip become important. Our observations favor the upper bound to the crossover length scale because the only evidence for systematic slickenline orientation variations occurs at the scale of the exposures of Corona Heights and Arkitsa faults (Figs. 4 and 6). Jackson and McKenzie (1999) suggest the variation in slickenline rake on the Arkitsa fault occurred due to a tectonic stress field rotation that caused a fault block rotational axis change through time. However, the amount of slip on the Corona Heights fault is much smaller so temporal variations in the displacement direction should be small, suggesting asperities at the exposure-scale cause the observed rotation. Slickenline rotations observed over meter distances elsewhere (e.g. Spudich et al., 1998 and references therein) could also correlate to the crossover length scale on other faults, though no comparison to the fault geometry is possible to verify this.

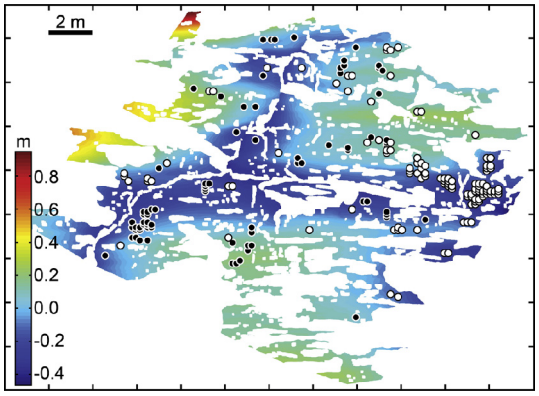

Fig. 7. Locations of slickenlines on the Corona Heights fault with rakes greater than one standard deviation from the mean rake measured with the curvature method. Black circles with white outlines are deflected upwards in this field of view, white circles with black outlines downwards.

Inelastic deformation is recorded by the presence of cataclasites that are developed adjacent to the polished slickenside of the Corona Heights fault (Fig. 1; Kirkpatrick et al., 2013). Fracturing and distributed cataclastic flow were the dominant deformation mechanisms during fault rock formation, which show the elastic limit of the rock was exceeded at multiple stages during the deformation history. Inelasticity may also have been due thermal weakening if frictional heating was significant (O'Hara, 2005; Rice, 2006; Reches and Lockner, 2010). The RMS roughness at the lower bound on the cross-over length scale ($L \sim 10^{-2}$ m) corresponds to the thickness (10^{-3} m) of the layer of relict silica gel identified by Kirkpatrick et al. (2013) and at the upper bound ($L \sim 10^{0}$ m) the RMS roughness is around 10^{-2} m which is approximately the thickness of the cataclasite in the fault core. The thicknesses of the fault core and principal slip zone may therefore provide a direct record of the crossover length scale.

5.2. Fault roughness scaling and deformation processes

The curvature of the Corona Heights and Arkitsa faults suggests that the fault surface roughness is organized into identifiable corrugations (Figs. 1, 4 and 6). Corrugations have long been recognized on fault surfaces in the field (e.g. Miller, 1922; Hancock and Barka, 1987; Jackson and McKenzie, 1999; Ferrill et al., 1999) and have also been recognized in LiDAR data (Jones et al., 2009). In exposure, corrugations spaced a few tens of centimeters apart are cut by synthetic shear fractures and smaller grooves, and can be seen to ride over larger amplitude asperities (Fig. 1c).

Corrugations on the fault surface are not recorded by the power spectral density of the Corona Heights fault, which shows no scaling break even though the tens of centimeter scale is well resolved (Fig. 1f). Some early studies suggested a break in the slope of the power spectral density of faults that corresponds to a change in the physical deformation processes (e.g. Power and Tullis, 1991; Lee and Bruhn, 1996). However, when the spectra are based on ground-based LiDAR data and the power at each wavelength averaged over thousands of calculations, the results yield self-affine power spectra with a single scaling exponent over the entire range of observed wavelengths from 10's of microns to 10's of kilometers (e.g. Candela et al., 2012).

As both the slickenline identification and the power spectral estimates stem from the same LiDAR data, the absence of a slickenline fingerprint on the power spectra is confusing. The difference can be attributed to the fact that power spectra are a reduction of information and do not capture the full the topographic information of the original dataset. For instance, there is no phase

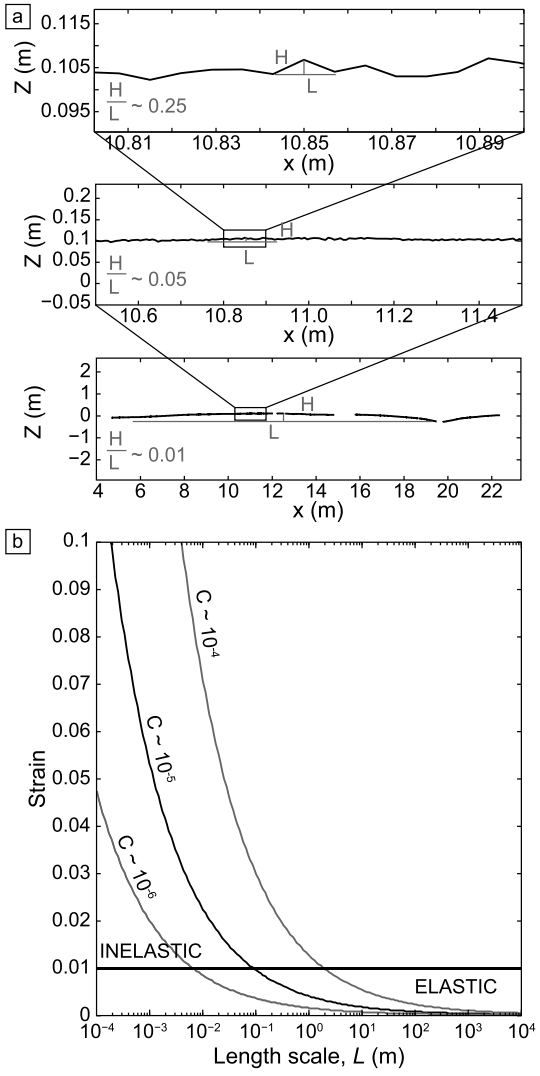

Fig. 8. a. Illustration of how the height:length ratio (H/L) of asperities changes as the scale of observation changes. The upper panel is a zoomed-in cross-sectional profile in the slip-parallel direction. The middle and lower panels are progressively zoomed out. Profiles are taken from the Corona Heights fault LiDAR point cloud shown in Fig. 2. b. Plot showing the strain required to compress asperities at a particular length scale as a function of length scale (see text for description). Above some critical length scale, the deformation can be accommodated elastically. Below the critical length scale, the elastic limit of rock is exceeded and the deformation is inelastic. The black line is calculated for $C = 1 \times 10^{-5}$ m^3, the approximate value of the power at 1 m wavelength in Fig. 1f. Grey lines show order of magnitude changes in C that are consistent with the variability in the prefactor.

information in the power spectra and therefore most interpretations implicitly infer random phase for a self-affine model.

We illustrate that a random-phase, self-affine model can differ from a surface with the identical, scale-free power spectrum, which displays distinctive, scale-dependent features using a synthetic self-affine model (Supplementary material). The synthetic fault has statistically the same shape, and analysis of the curvature shows a similar distribution of slickenline rakes, but the fault does not exhibit any recognizable corrugations. We conclude that the corrugations are a distinctive feature, however, a power law with constant scaling exponent is still an accurate representation of the roughness across scales.

We reconcile these observations by recognizing that multiple processes contribute to deformation during fault slip, but that underlying each process is brittle failure, which imposes a consistent limit on the resultant roughness (Fig. 9). Cataclastic deformation during faulting involves grain-scale processes such as

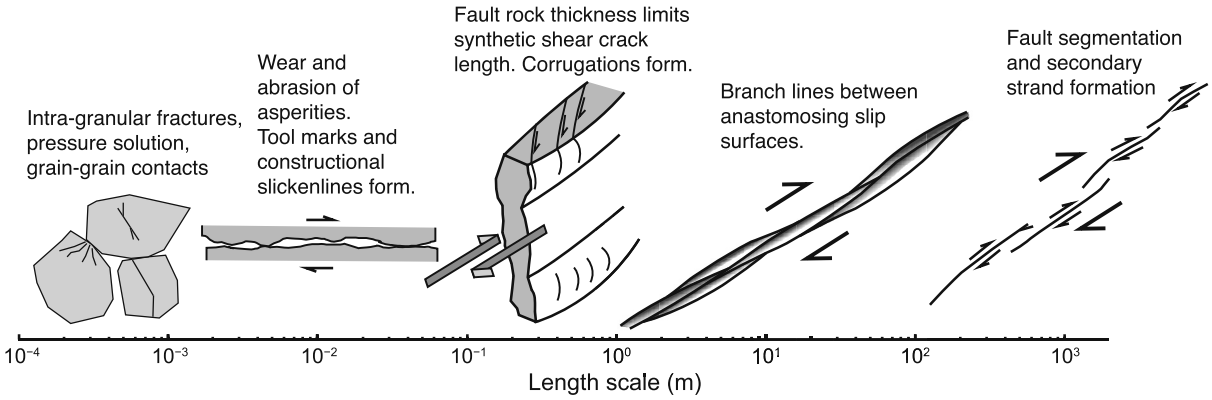

Fig. 9. Diagram illustrating the range of processes that contribute to fault roughness that operate at various scales. All of these processes may be expected to influence fault geometry during deformation, yet the geometry remains constant.

intra-granular fracturing, wear and abrasion during frictional sliding, and fault core-scale processes such as the development of subsidiary shear fractures and distributed cataclastic flow. Linkage of segments through fracture to form mature structures occurs at longer length scales. Despite each of these processes operating at fundamentally different length scales, they all involve some form of inelastic yielding and so are functions of the elastic limit of the rock. The relatively narrow range of observed roughness values at the meter-scale corresponds to 0.1–1% aspect ratios as might be expected for a process controlled by the elastic limit (Brodsky et al., 2011). We speculate that the self-affine scaling of fault roughness (Hurst exponent $\sim$0.8) might result from scale-dependence of the failure strength of rocks. Reduced failure thresholds at large scales could result in smaller values of roughness (H/L) at large scales, as observed.

6. Conclusions

Slickenline rakes measured in LiDAR point clouds of three fault surfaces vary by only a few degrees over the extent of the exposures we studied. As the slickenlines are kinematic indicators, the results demonstrate that slip directions are not influenced by fault geometry at small scales. Slip directions are therefore insensitive to any local variations in the shear traction directions caused by elastic asperity contact at scales up to around a few meters. We suggest this observation shows that asperities on the fault surface were in an inelastic regime at short length scales. Roughness measurements indicate a crossover to elastic asperity deformation occurs at length scales of $\sim 10^{-2}$ to 10^{0} m. This crossover captures the length scale of a strength asperity on the fault during slip. The RMS roughness at these lengths corresponds to fault rock thickness, which may therefore record the crossover length scale. The characteristic self-affine shape of fault surfaces is the product of multiple processes that act at a range of scales that are all forms of inelastic deformation governed by the elastic limit of the rock. The commonly observed Hurst exponents below 1 might be derived from the fact that rocks fail more easily at larger scales.

Acknowledgements

We thank Richard Jones for generously sharing the Arkitsa LiDAR data. We also thank Nicholas van der Elst for making the data collection at Corona Heights possible and Eric Dunham for helpful discussions of the results of this study. Constructive reviews by Ze'ev Reches and Joe Allen greatly improved the manuscript. This work was supported in part by NSF grant EAR-0948740.

Appendix A. Supplementary material

Supplementary material related to this article can be found online at http://dx.doi.org/10.1016/j.epsl.2014.09.040.

References

Angelier, J., 1989. From orientation to magnitudes in paleostress determinations using fault slip data. J. Struct. Geol. 11 (1), 37–50.
Archard, J., 1953. Contact and rubbing of flat surfaces. J. Appl. Phys. 24 (8), 981–988.
Bergbauer, S., Pollard, D.D., 2003. How to calculate normal curvatures of sampled geological surfaces. J. Struct. Geol. 25 (2), 277–289. http://dx.doi.org/10.1016/S0191-8141(02)00019-6.
Blake Jr., M.C., Howell, D.G., Jayko, A.S., 1984. Tectonostratigraphic terranes of the San Francisco Bay region. In: Blake Jr., M.C. (Ed.), Franciscan Geology of Northern California. In: Pacific Section S.E.P.M., vol. 43, pp. 5–22.
Blake, M.C. Jones, D.L. Graymer, R.W., 2000. Geologic map and map database of parts of Marin, San Francisco, Alameda, Contra Costa, and Sonoma counties, California. US Department of the Interior, US Geological Survey.
Bott, M.H.P., 1959. The mechanics of oblique slip faulting. Geol. Mag. 96 (02), 109–117.
Brodsky, E.E., Gilchrist, J.G., Sagy, A., Colletini, C., 2011. Faults smooth gradually as a function of slip. Earth Planet. Sci. Lett. 302, 185–193. http://dx.doi.org/10.1016/j.epsl.2010.12.010.
Brown, S.R., Scholz, C.H., 1985. Broad bandwidth study of the topography of natural rock surfaces. J. Geophys. Res. 90 (B14), 12575–12582.
Caine, J.S., Bruhn, R.L., Forster, C.B., 2010. Internal structure, fault rocks, and inferences regarding deformation, fluid flow, and mineralization in the seismogenic Stillwater normal fault, Dixie Valley, Nevada. J. Struct. Geol. 32 (11), 1576–1589. http://dx.doi.org/10.1016/j.jsg.2010.03.004.
Candela, T., Renard, F., Bouchon, M., Marsan, D., Schmittbuhl, J., Voisin, C., 2009. Characterization of fault roughness at various scales: implications of three-dimensional high resolution topography measurements. Pure Appl. Geophys. 166, 1817–1851. http://dx.doi.org/10.1007/s00024-009-0521-2.
Candela, T., Renard, F., Schmittbuhl, J., Bouchon, M., Brodsky, E.E., 2011a. Fault slip distribution and fault roughness. Geophys. J. Int. 187 (2), 959–968. http://dx.doi.org/10.1111/j.1365-246X.2011.05189.x.
Candela, T., Renard, F., Bouchon, M., Schmittbuhl, J., Brodsky, E.E., 2011b. Stress drop during earthquakes: effect of fault roughness scaling. Bull. Seismol. Soc. Am. 101, 2369–2387. http://dx.doi.org/10.1785/0120100298.
Candela, T., Renard, F., Klinger, Y., Mair, K., Schmittbuhl, J., Brodsky, E.E., 2012. Roughness of fault surfaces over nine decades of length scales. J. Geophys. Res. 117, B08409. http://dx.doi.org/10.1029/2011JB009041.
Chambon, G., Schmittbuhl, J., Corfdir, A., Orellana, N., Diraison, M., Géraud, Y., 2006. The thickness of faults: from laboratory experiments to field scale observations. Tectonophysics 426 (1), 77–94. http://dx.doi.org/10.1016/j.tecto.2006.02.014.
Chester, F.M., Chester, J.S., 1998. Ultracataclasite structure and friction processes of the Punchbowl fault, San Andreas system, California. Tectonophysics 295 (1), 199–221.
Chester, F.M., Chester, J.S., 2000. Stress and deformation along wavy frictional faults. J. Geophys. Res. 105 (B10), 23,421–23,430. http://dx.doi.org/10.1029/2000JB900241.
Cowie, P.A., Scholz, C.H., 1992. Displacement-length scaling relationship for faults: data synthesis and discussion. J. Struct. Geol. 14 (10), 1149–1156.
Di Toro, G., Pennacchioni, G., 2004. Superheated friction-induced melts in zoned pseudotachylytes within the Adamello tonalites (Italian Southern Alps). J. Struct. Geol. 26 (10), 1783–1801. http://dx.doi.org/10.1016/j.jsg.2004.03.001.

Dieterich, J.H., Smith, D.E., 2009. Nonplanar faults: mechanics of slip and off-fault damage. Pure Appl. Geophys. 166, 1799–1815. http://dx.doi.org/10.1007/s00024-009-0517-y.

Doblas, M., 1998. Slickenside kinematic indicators. Tectonophysics 295 (1), 187–197.

Dunham, E.M., Belanger, D., Cong, L., Kozdon, J.E., 2011. Earthquake ruptures with strongly rate-weakening friction and off-fault plasticity. Part 2: Nonplanar faults. Bull. Seismol. Soc. Am. 101 (5), 2308–2322. http://dx.doi.org/10.1785/0120100076.

Fang, Z., Dunham, E.M., 2013. Additional shear resistance from fault roughness and stress levels on geometrically complex faults. J. Geophys. Res., Solid Earth 118, 3642–3654. http://dx.doi.org/10.1002/jgrb.50262.

Ferrill, D.A., Stamatakos, J.A., Sims, D., 1999. Normal fault corrugation: implications for growth and seismicity of active normal faults. J. Struct. Geol. 21 (8), 1027–1038.

Fondriest, M., Smith, S.A., Candela, T., Nielsen, S.B., Mair, K., Di Toro, G., 2013. Mirror-like faults and power dissipation during earthquakes. Geology 41 (11), 1175–1178.

Gephart, J.W., 1990. Stress and the direction of slip on fault planes. Tectonics 9 (4), 845–858.

Greenwood, J.A., Williamson, J.B.P., 1966. Contact of nominally flat surfaces. Proc. R. Soc. Lond. Ser. A, Math. Phys. Sci. 295 (1442), 300–319.

Hancock, P.L., Barka, A.A., 1987. Kinematic indicators on active normal faults in western Turkey. J. Struct. Geol. 9, 573–584.

Jackson, J., McKenzie, D., 1999. A hectare of fresh striations on the Arkitsa Fault, central Greece. J. Struct. Geol. 21 (1), 1–6.

Jones, R.R., Kokkalas, S., McCaffrey, K.J.W., 2009. Quantitative analysis and visualization of nonplanar fault surfaces using terrestrial laser scanning (LIDAR)—the Arkitsa fault, central Greece, as a case study. Geosphere 5 (6), 465–482. http://dx.doi.org/10.1130/GES00216.1.

Katz, O., Reches, Z.E., Baer, G., 2003. Faults and their associated host rock deformation. Part I. Structure of small faults in a quartz–syenite body, southern Israel. J. Struct. Geol. 25 (10), 1675–1689. http://dx.doi.org/10.1016/S0191-8141(03)00011-7.

Kirkpatrick, J.D., Rowe, C.D., White, J.C., Brodsky, E.E., 2013. Silica gel formation during fault slip: evidence from the rock record. Geology 41 (9), 1015–1018.

Lee, J.J., Bruhn, R.L., 1996. Structural anisotropy of normal fault surfaces. J. Struct. Geol. 18 (8), 1043–1059.

Lyakhovsky, V., Sagy, A., Boneh, Y., Reches, Z.E., 2014. Fault wear by damage evolution during steady-state slip. Pure Appl. Geophys. 1 (15). http://dx.doi.org/10.1007/s00024-014-0787-x.

Marshall, S.T., Morris, A.C., 2012. Mechanics, slip behavior, and seismic potential of corrugated dip-slip faults. J. Geophys. Res. 117, B03403. http://dx.doi.org/10.1029/2011JB008642.

Means, W.D., 1976. Stress and Strain: Basic Concepts of Continuum Mechanics for Geologists, 4th edition. Springer-Verlag.

Miller, William J., 1922. Intraformational corrugated rocks. J. Geol. 30 (7), 587–610.

Murchey, B., 1984. Biostratigraphy and lithostratigraphy of chert in the Franciscan Complex, Marin Headlands, California. In: Blake Jr., M.C. (Ed.), Franciscan Geology of Northern California. In: Pacific Section S.E.P.M., vol. 43, pp. 51–70.

Murchey, B.L., Jones, D.L., 1984. Age and significance of chert in the Franciscan Complex in the San Francisco Bay Region. In: Blake Jr., M.C. (Ed.), Franciscan Geology of Northern California. In: Pacific Section S.E.P.M., vol. 43, pp. 23–30.

O'Hara, K., 2005. Evaluation of asperity-scale temperature effects during seismic slip. J. Struct. Geol. 27 (10), 1892–1898.

Persson, B.N., 2001. Theory of rubber friction and contact mechanics. J. Chem. Phys. 115 (8), 3840–3861.

Petit, J.P., 1987. Criteria for the sense of movement on fault surfaces in brittle rocks. J. Struct. Geol. 9 (5), 597–608.

Pollard, D.D., Saltzer, S.D., Rubin, A.M., 1993. Stress inversion methods: are they based on faulty assumptions? J. Struct. Geol., (ISSN 0191-8141) 15 (8), 1045–1054.

Power, W.L., Tullis, T.E., 1991. Euclidean and fractal models for the description of rock surface roughness. J. Geophys. Res. 96 (B1), 415–424.

Power, W.L., Tullis, T.E., Brown, S.R., Boitnott, G.N., Scholz, C.H., 1987. Roughness of natural fault surfaces. Geophys. Res. Lett. 14 (1), 29–32.

Power, W.L., Tullis, T.E., Weeks, J.D., 1988. Roughness and wear during brittle faulting. J. Geophys. Res., Solid Earth 93 (B12), 15268–15278.

Reches, Z., 1987. Determination of the tectonic stress tensor from slip along faults that obey the Coulomb yield condition. Tectonics 6, 849–861.

Reches, Z.E., Lockner, D.A., 2010. Fault weakening and earthquake instability by powder lubrication. Nature 467 (7314), 452–455.

Renard, F., Voisin, C., Marsan, D., Schmittbuhl, J., 2006. High resolution 3D laser scanner measurements of a strike-slip fault quantify its morphological anisotropy at all scales. Geophys. Res. Lett. 33, L04305. http://dx.doi.org/10.1029/2005GL025038.

Resor, P.G., Meer, V.E., 2009. Slip heterogeneity on a corrugated fault. Earth Planet. Sci. Lett. 288, 483–491. http://dx.doi.org/10.1016/j.epsl.2009.10.010.

Rice, J.R., 2006. Heating and weakening of faults during earthquake slip. J. Geophys. Res. 111, B05311. http://dx.doi.org/10.1029/2005JB004006.

Ritz, E., Pollard, D.D., 2012. Stick, slip, and opening of wavy frictional faults: a numerical approach in two dimensions. J. Geophys. Res. 117, B03405. http://dx.doi.org/10.1029/2011JB008624.

Sagy, A., Brodsky, E.E., 2009. Geometric and rheological asperities in an exposed fault zone. J. Geophys. Res. 114, B02301. http://dx.doi.org/10.1029/2008JB005701.

Sagy, A., Brodsky, E.E., Axen, G.J., 2007. Evolution of fault-surface roughness with slip. Geology 35, 283–286. http://dx.doi.org/10.1130/G23235A.1.

Saucier, F.J., Humphreys, E.D., Weldon, R.J., 1992. Stress near geometrically complex strike-slip faults: application to the San Andreas fault near Cajon Pass, southern California. J. Geophys. Res. 97 (B4), 5081–5094. http://dx.doi.org/10.1029/91JB02644.

Scholz, C.H., 1987. Wear and gouge formation in brittle faulting. Geology 15 (6), 493–495.

Scholz, C.H., Engelder, J.T., 1976. The role of asperity indentation and ploughing in rock friction—I: Asperity creep and stick-slip. Int. J. Rock Mech. Min. Sci. Geomech. Abstr. 13 (5), 149–154. Pergamon.

Shen, Z.K., Sun, J., Zhang, P., et al., 2009. Slip maxima at fault junctions and rupturing of barriers during the 2008 Wenchuan earthquake. Nat. Geosci. 2 (10), 718–724.

Shi, Z., Day, S.M., 2013. Rupture dynamics and ground motion from 3D rough-fault simulations. J. Geophys. Res., Solid Earth 118 (3), 1122–1141. http://dx.doi.org/10.1002/jgrb.50094.

Siman-Tov, S., Aharonov, E., Sagy, A., Emmanuel, S., 2013. Nanograins form carbonate fault mirrors. Geology 41 (6), 703–706.

Spudich, P., Guatteri, M., Otsuki, K., Minagawa, J., 1998. Use of fault striations and dislocation models to infer tectonic shear stress during the 1995 Hyogo-ken Nanbu (Kobe) earthquake. Bull. Seismol. Soc. Am. 88 (2), 413–427.

Twiss, R.J., Unruh, J.R., 1998. Analysis of fault slip inversions: do they constrain stress or strain rate? J. Geophys. Res., Solid Earth 103 (B), 12205. http://dx.doi.org/10.1029/98JB00612.